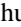




Switchable topological phase transition and nonlinear optical properties in a ReC₂H monolayerChunmei Zhang ^{1,*}, Hanqi Pi ^{2,*}, Liqin Zhou ^{2,*}, Si Li ¹, Jian Zhou ³, Aijun Du ⁴, and Hongming Weng ^{2,5,‡}¹*School of Physics, Northwest University, Xi'an 710069, China*²*Beijing National Laboratory for Condensed Matter Physics and Institute of Physics, Chinese Academy of Sciences, Beijing 100190, China*³*Center for Alloy Innovation and Design, State Key Laboratory for Mechanical Behavior of Materials, Xi'an Jiaotong University, Xi'an 710049, China*⁴*School of Chemistry and Physics, Queensland University of Technology, Gardens Point Campus, Brisbane, QLD 4001, Australia*⁵*Songshan Lake Materials Laboratory, Dongguan, Guangdong 523808, China*

(Received 11 March 2022; accepted 31 May 2022; published 9 June 2022)

The topological phase transitions (TPTs) in three-dimensional compounds have attracted great attention in both condensed-matter physics and applied physics. Compared to the TPT in bulk structures, TPTs in noncentrosymmetric two-dimensional materials are less common and require further study. This work explores an inversion asymmetry structure, ReC₂H monolayer by first-principle calculation. We show that it undergoes two TPTs at the critical biaxial strain of 2.3 and 7.8%, where the material transforms from normal insulator to Z₂ topological insulator and back to normal insulator, respectively. In the first TPT, the band inversion occurs at the generic momentum. The second one occurs at the high-symmetric *K* point, identified by an exchange in the components (or irreducible representations) of the wave functions. These quantities are challenging to be detected using experimental techniques, such as angle-resolved photoemission spectroscopy. Since the nonlinear optical (NLO) response is very sensitive to the components and symmetries of the engaged bands, we study the shift current generation during the two aforementioned TPTs. We find that in both TPTs, the shift vectors change sign around momenta where the band gap closes and reopens. By considering the overall contribution of shift vectors weighted by the absorption rate in the whole Brillouin zone, the shift current may keep its direction under band inversion. This work offers the insight that a scrutinized examination is highly demanded in utilizing the shift current to detect TPT.

DOI: [10.1103/PhysRevB.105.245108](https://doi.org/10.1103/PhysRevB.105.245108)**I. INTRODUCTION**

Topological materials are classified as topological insulators (TIs), topological crystalline insulators, and topological semimetals (TSMs) according to different nontrivial topological invariants. Among them, TIs that possess a Z₂ invariant are protected by time-reversal symmetry and the corresponding gapless surface/edge Dirac state. TSMs have a conduction band crossing with a valence band at the Fermi level, and their crossing points can be identified by the topological charge invariant. Typical TSMs, including Dirac semimetals and Weyl semimetals (WSMs), can be viewed as critical phases during the topological phase transition (TPT) between the topological trivial (Z₂ = 0) and nontrivial (Z₂ = 1) states proposed by Murakami [1]. TPT can be driven by external stimuli such as electric field [2], magnetization [3], mechanical strain, hydrostatic pressure [4,5], etc. In a simple model, all these approaches modulate the effective mass parameter "*m*" [1] near the Fermi level. Quite a few exotic physical phenomena occur during TPT, which can be used to identify topological materials in practice. For example, when the temperature

drops, ZrTe₅ and HfTe₅ will experience insulator-metal transition and enhanced diamagnetism [6]. Exploring more unique and intriguing phenomena during TPT is significant in understanding and developing their potential applications and actual usage. As most optical processes are determined by interband transitions between the valence and conduction bands, one may expect that a TPT can be traced by inspecting optical responses [7–9]. In addition, the optical approach is advantageous for its noncontacting and highly tunable nature, which does not require mechanical or electrochemical methods to contact the systems during operation directly. Moreover, tuning of light frequency, incident angle, polarization, and intensity can be easily performed without directly affecting the samples. Hence, it is less likely to cause lattice damage and rarely introduces unwanted impurities.

One of the intriguing optical responses in noncentrosymmetric systems is the bulk photovoltaic effect (BPVE) [10–12], which yields steady-state electric current under homogeneous optical illumination [13]. This nonlinear optical (NLO) approach can generate current while avoiding the traditional complicated fabrication process of heterostructures, such as *p-n* junction. It offers great potential in energy harvesting, photodetection, and rectification [14]. Microscopically, photon irradiation generates electron-hole pairs via electronic interband transition [7], which is governed by the geometry features of wave functions such as Berry connection and

*These authors contributed equally to this work.

†chunmeizhang@nwu.edu.cn

‡hmweng@iphy.ac.cn

quantum metric dipoles in the momentum space [15–17]. In time-reversal symmetric systems, the primary BPVE is the generation of shift current under linearly polarized light, which arises from the displacement of carrier positions during the interband optical excitation [18]. Thus, the shift current reflects the topological nature via interband Berry connection. Described by the formula composed of Berry connection, the shift vector that evaluates the k -resolved shift-current generation is a gauge-invariant quantity. It can be interpreted as the difference of intracell coordinates between the valence and conduction bands, which is odd and usually flips its sign under band inversion during TPT [18,19]. As the net shift current is the product of absorption rate and shift vector, one may expect that the change of photocurrent magnitude and/or direction could be utilized to detect band inversion during TPT [7].

Generally, TIs possess intrinsic band inversion and enhanced Berry connection near their band gap [20–24], which could significantly boost their linear [24] and nonlinear [7,9] optical responses. In addition, at the critical TPT point, the electronic joint density of states (JDOS) scales with ω^2 (ω being the frequency of the incident light) [21]. Simultaneously, it also leads to the singularity of the Berry connection owing to a zero band gap. Hence, the shift-current responses in the low-energy limit may be anomalously large [21,22]. Similar design principles for searching shift-current materials aim at discovering semi-Dirac type Hamiltonians and/or strong JDOS singularity [25]. From the materials realization perspective, a large shift current has been experimentally detected to be $154 \pm 17 \mu\text{A}/\text{V}^2$ (at the photon energy $\hbar\omega = 0.12 \text{ eV}$) in TaAs [21], consistent with the above analyses. In addition, Xu *et al.* [23] have theoretically predicted 46 WSM candidate materials based on high-throughput calculations, and they show that most of them exhibit giant shift-current conductance.

The above topological viewpoint offers a route to the rational design of large NLO materials. However, there are still several problems that remain unsolved: (i) Most investigations are performed on three-dimensional (3D) WSMs. Considering that two-dimensional (2D) materials often show stronger van Hove singularities in their density of states at the band edge [26], a much-enhanced shift current could be expected. Unfortunately, 2D noncentrosymmetric TIs with well-controlled TPT are poorly studied either from the material design perspective or in terms of the NLO effects. (ii) Since shift current is the overall contribution of shift vectors weighted by the absorption rate in the whole Brillouin zone (BZ), the reversal of the shift vector direction at some momenta does not guarantee the direction change of the shift current, especially when the band inversion momenta barely contribute to the shift current. Nevertheless, these issues have not been carefully discussed.

In this work, we address these problems based on density-functional theory (DFT) calculations, by investigating a 2D system, a single-side hydrogenated rhenium carbide (ReC_2H) monolayer which belongs to the C_{3v} symmetry group. The inversion asymmetry, together with strong spin-orbit coupling (SOC), gives rise to giant Rashba spin splitting in the system's electronic bands at generic k points. We find that the SOC band gap is direct, controllable, and can be effectively tuned by a biaxial mechanical strain. In detail, this system experiences two TPTs under intermediate biaxial strains, namely, from a normal insulator to a Z_2 -TI at a critical strain (ε_{c1})

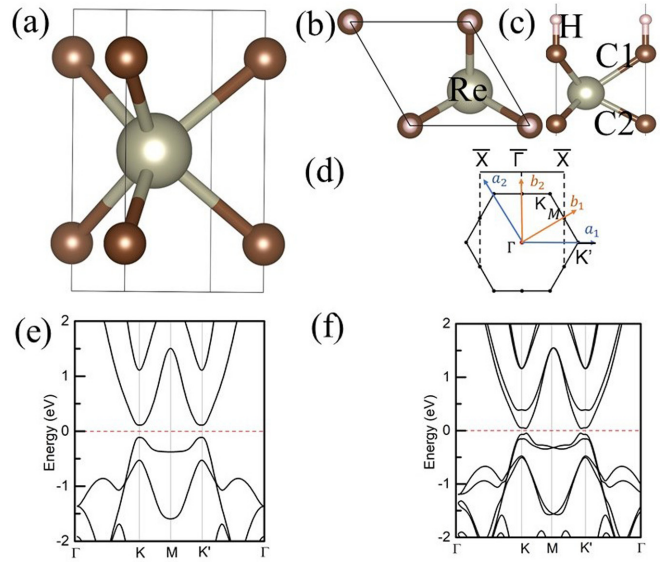


FIG. 1. (a) Side view of $1 \times 1 \times 2$ supercell ReC_2 compound. (b), (c) top and side views of ReC_2H monolayer, where C1 and C2 are labeled to differentiate C atoms. (d) The 2D BZ and the projected one-dimensional BZ along the armchair direction. The band structure of ReC_2H monolayer was calculated at the GGA level of theory (e) without and (f) with SOC. The Fermi level is denoted by the red dashed horizontal line.

around 2.3%, and back to a normal insulator when strain exceeds 7.8% (ε_{c2}). During the two TPTs, the dependence of shift current is also analyzed. The shift-current direction is unchanged across ε_{c1} , while it reverses at ε_{c2} . This has been analyzed and it is noted that the band inversion reverses the shift vector locally in the momentum space while the shift current is determined by its integration weighted by absorption rate.

II. RESULTS

A. Geometric structure of ReC_2H monolayer

The experimental crystal structure of ReC_2 [27] is shown in Fig. 1(a). It crystallizes in the hexagonal structure with the space group of $\bar{P}6m2$ (No. 187) and presents trivial metallic conductivity [27]. When it is H-passivated on a single side, the single-layer ReC_2H [Figs. 1(b) and 1(c)] belongs to the space group $P3m1$ (No. 156) without inversion symmetry. The optimized lattice constant is 3.002 \AA . The single-sided H passivation breaks the out-of-plane mirror symmetry.

From a material realization perspective, hydrogenation engineering has been experimentally fabricated and theoretically investigated extensively [28], i.e., atomic-scale patterning of H on various bulk or 2D semiconductors such as Si [29,30], Ge [31,32], etc. In the current system, H atoms passivate the C dangling bonds, which not only act as a resist in analogy to that used in optical lithography [31] but also tune the chemical potential. The H adsorption energy is calculated to be -1.094 eV/atom , indicating strong chemical bonding. In addition, the crystal structure of the ReC_2H monolayer resembles that of the 2H-MoS_2 , which has been synthesized by chemical vapor deposition [33,34]. To examine its dynamic

stability, we present our calculated phonon spectra in Fig. S1(a) and S1(b) [35], where no imaginary frequencies can be seen over the whole BZ. The *ab initio* molecular-dynamics (AIMD) simulations are further carried out for 10 ps at 300 and 500 K [Figs. S1(c) and S1(d) [35]]. No evidence of structural destruction can be observed, suggesting thermal stability. Hence, the structure belongs to a local minimum on the potential-energy landscape, which is protected by a high-energy barrier against structural transformation or destruction. There is a good synthesis possibility in experiments.

B. Electronic structure analysis

We first calculate the band structure of ReC₂H without SOC using generalized gradient approximation (GGA) functional and plot it along the high-symmetric k path in Fig. 1(e), which indicates that it is a semiconductor with a band gap of about 0.3 eV. The bands near the Fermi level are mainly contributed by C2 (unsaturated carbon) p_z orbital and Re d_{xy} , $d_{x^2-y^2}$ orbitals. Including SOC would break the spin rotational symmetry and trigger Rashba-like spin splitting at generic k points [36] [Fig. 1(f)]. Note that the spin degeneracy at time-reversal invariant momenta Γ and M results from Kramers degeneracy. The Rashba splitting greatly reduces the band gap to ~ 0.1 eV. This would reduce the potential critical field for TPT. Thus, we mainly focus on the discussion of the electronic structure with SOC in our following discussions.

When the space-inversion symmetry is broken, the topological invariant Z_2 for a band insulator with time-reversal symmetry can be obtained through the evolution of Wannier charge centers of occupied states, as shown in Fig. S4 [35,37–39]. The calculated Z_2 invariant as a function of mechanical strains is shown in Fig. 2, with part of the valence- and conduction bands along the $\Gamma - K - M$ path near the K point. The whole band structures are plotted in Fig. S3 [35]. We find that the bands near the Fermi level are mainly from Re- d_{xy} , Re- $d_{x^2-y^2}$ (weighted by green curve), and C2 p_z orbitals (weighted by red curve) [in Figs. 2(a)–2(l)]. As tensile strain increases, the band gap closes and reopens twice, indicating two TPTs at $\varepsilon_{c1} = 2.3\%$ and $\varepsilon_{c2} = 7.8\%$, respectively. Detailed analysis reveals that the first TPT occurs at a generic momentum around the path $K - M$, and the second one is at K . Before ε_{c2} , the irreducible representations (IRs) for valence-band maximum (VBM) and conduction-band minimum (CBM) are GM5 and GM6, respectively. The energy orders of them are inverted at ε_{c2} . More details for the IRs of bands at K are listed in Table S1. It should be noted that there is also band exchange in IRs around a strain of 7% [Fig. 2(i)] in the two conduction bands. Although it does not affect the topological property of the occupied states, it enables the second TPT.

The band inversion identified by IRs of related bands is seen in the second TPT, but this method fails in understanding the first TPT since the CBM and VBM at generic momenta have the same IRs. On the other hand, the orbital components resemble each other in the first TPT, as shown in Table S3 [35]. Therefore, the first TPT is not easily captured by these two methods, although Z_2 changes from 0 to 1. The strain-induced TPT of ReC₂H can be understood with the theory proposed by Murakami *et al.* [1] Around the gap-closing point, the $\mathbf{k} \cdot \mathbf{p}$ Hamiltonian reduces to a two-component

Hamiltonian, $H = m\sigma_z + (k_x - k_{0x})\sigma_x + (k_y - k_{0y})\sigma_y$. Taking the first TPT as an example, the mass parameter m changes sign around a strain of 2.3%, which is accompanied by a TPT. The TPT point is located at (k_{0x}, k_{0y}) when m equals to 0. In general, the location of the TPT point can be at any generic momentum. According to the space group $P3m1$ of this system, in the first TPT, there are altogether 12 gap-closing points that are related by C_3 rotation, mirror symmetry, and time-reversal symmetry. In the second TPT, the gap-closing points are at K and K' .

As the gapless topological boundary state is an essential character for a TI belonging to the nontrivial Z_2 classification, we further calculate the one-dimensional (1D) edge states. Both armchair [Figs. 2(m)–2(o)] and zigzag (Fig. S5 [35]) edge states are plotted for $\varepsilon = 0.9, 4,$ and 10% , respectively. The 1D Dirac cones of the edge state for 0.9 and 10% tensile ReC₂H monolayers connect the valence band only, indicating the system is topologically trivial with $Z_2 = 0$. On the contrary, two helical edge states protected by time-reversal symmetry clearly appear at $\varepsilon = 4\%$, where the Dirac cone at time-reversal invariant momentum \bar{X} is demanded by Kramers degeneracy and its two branches connecting the projections of bulk valence- and conduction bands, respectively. This demonstrates the nontrivial topology for $Z_2 = 1$.

C. Shift-current variation under topological phase transition

As both theory and experiment demonstrate that topological materials can exhibit large NLO responses [7,40], we further consider the influence of band topology on the shift current. In the current system, there are two TPTs under tensile strain; one has explicit band inversion while the other does not. It would be interesting to investigate the TPTs' influence on the NLO responses.

The inversion symmetry-broken monolayer ReC₂H has a mirror plane perpendicular to $\hat{\mathbf{x}}$, which is along the zigzag direction. The synergistic effects of mirror reflection and C_3 rotation lead to four independent nonvanishing shift-current response tensors, namely, in-plane $\sigma^{yyy} = -\sigma^{xxx} = -\sigma^{xyx}$ and out-of-plane $\sigma^{zxx} = \sigma^{zyy}$, σ^{zzz} , $\sigma^{xxz} = \sigma^{yyz}$. In this 2D system, since the out-of-plane conductivity component is not a well-defined quantity, we mainly focus on the discussion of the in-plane component σ^{yyy} . Around the first and second TPTs, σ^{yyy} variation under incident photon energy is calculated and shown in Figs. 3(a) and 3(b), respectively. It is noticed in both figures that the first peak of σ^{yyy} is mainly contributed by the transitions between the bands around K , since the corresponding photon energy is comparable with the direct band-gap value around K in Fig. 2.

Across the first TPT, the incident photon energy of the first σ^{yyy} peak decreases continuously, while the peak value increases with strain from 0 to 2.3% and then reduces after ε_{c1} . The maximum value reaches $600 \text{ \AA} \cdot \mu\text{A}/\text{V}^2$ (at $\hbar\omega = 0.070 \text{ eV}$ and $\varepsilon_{c1} = 2.3\%$). Before and after this TPT, the sign of σ^{yyy} remains unchanged. When ε increases from 0.9 to 2.3%, the band gap at the K point decreases steadily, which contributes most to the first peak of σ^{yyy} , making the magnitude of the first peak increase steadily. After ε_{c1} (2.3%), the main contribution point moves away from the K point slightly, which should have a smaller adsorption rate

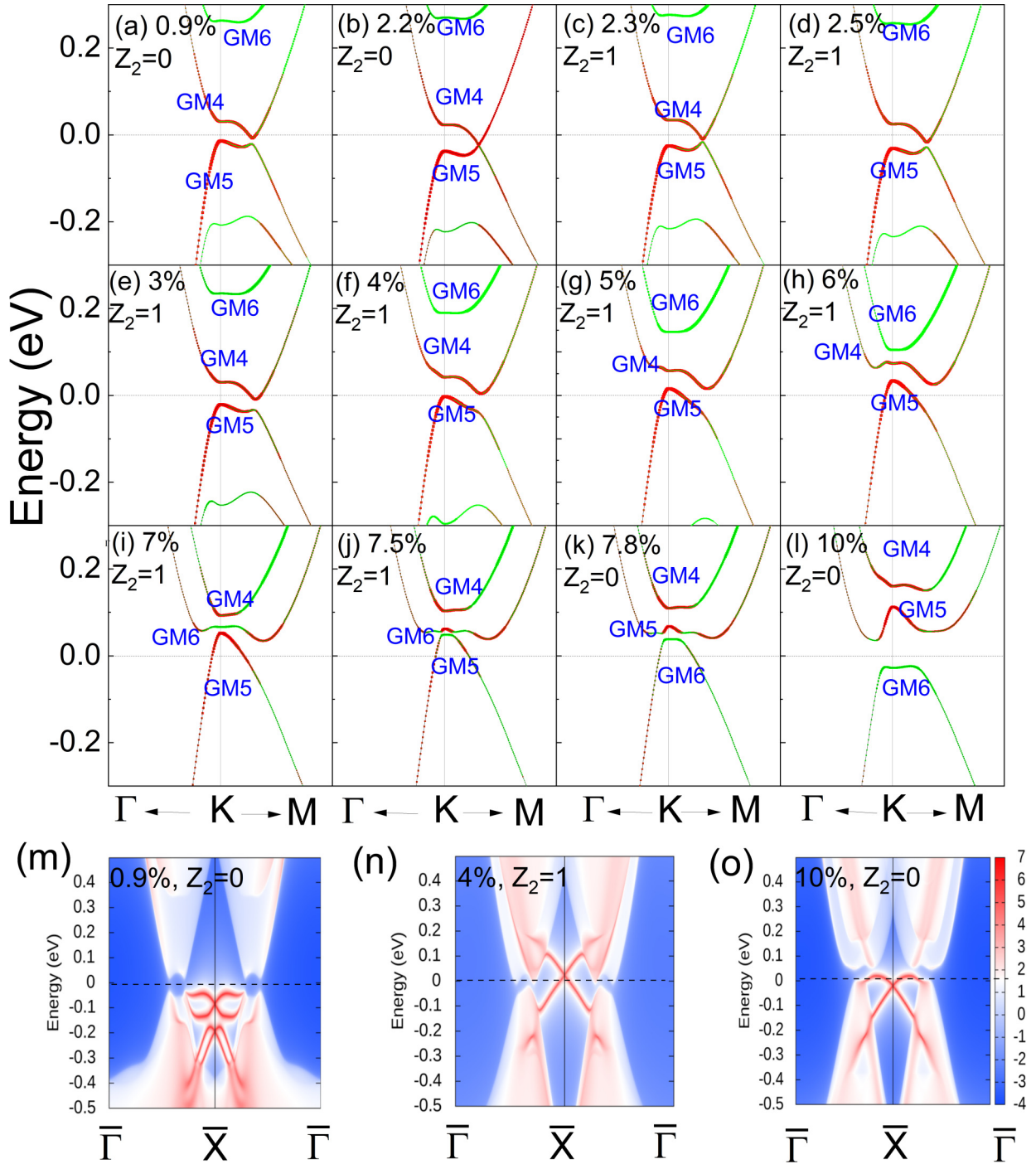


FIG. 2. [(a)–(l)] Band structure and Z_2 invariant for ReC₂H monolayer under 0.9–10% strain. The red curve represents the weight of C2 p_z orbitals, and the green curve denotes the weight from Re $d_{xy}, d_{x^2-y^2}$ orbitals. The band structure is calculated along the high-symmetry path $\Gamma - K - M$ around K . (m)–(o) The 1D armchair edge states of 0.9, 4, and 10% tensile ReC₂H monolayer. The Fermi level is marked by the black dashed line.

compared with the K point. This can be inferred from Table S2 [35] that the band gap at the K point is slightly smaller than the incident energy of the first peak of σ^{yy} . Thus, the magnitude of the first peak of σ^{yy} decreases after ε_{c1} .

On the other hand, around the second TPT (6–12%), σ^{yy} peak value decreases from $\sim 500 \text{ \AA} \cdot \mu A/V^2$ ($\varepsilon = 6.0\%$) to $\sim 70 \text{ \AA} \cdot \mu A/V^2$ ($\varepsilon = 7.8\%$). After the second TPT, σ^{yy} reverses its sign and increases its value from -150 to

$\sim -200 \text{ \AA} \cdot \mu A/V^2$ (at $\varepsilon = 10\%$) gradually. Before the second TPT, the first peak value of σ^{yy} keeps decreasing and the peak frequency shifts to higher energies from $\varepsilon = 7$ to 7.8%. This counterintuitive shift-current value changes should be noted. The reason is that the first peak position of σ^{yy} is not exactly located at K but slightly away from the K point. In structures with ε from 5 to 7%, the highest valence band and the lowest conduction band are almost parallel in a small

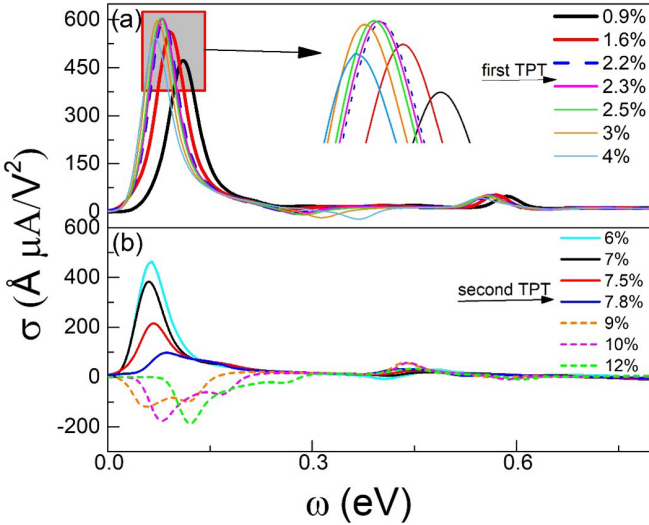


FIG. 3. Shift-current conductance σ^{shy} around the (a) first and (b) second TPT under different strains.

region on the K - M path which results in a large JDOS and a large contribution to shift current. Similarly, under ε from 7 to 7.8%, transitions between the highest valence band and the second-lowest conduction band around the K point have a more sizable contribution compared to the band edge (inferred from Table S2 [35]), which shifts the peak frequency value to the gap between the former mentioned two bands and reduces the intensity of shift current.

As the intensity of the shift current is inversely proportional to the magnitude of the gap, the shift current usually behaves divergently near TPT at zero frequency. However, here, the shift current in the structures with ε from 0.9 to 2.2% mostly comes from the K point and around, where the gap monotonically decreases but never closes, resulting in the vanishing shift current at the zero-frequency limit. This explanation also applies to the vanishing value at the zero-frequency limit for the second TPT.

We further move to analyze the band topological effect on the shift-current direction. As described in the Methods section, the shift current can be expressed as the integral of the product of the absorption rate $|r_{mn}^b|^2 \delta(\omega_{nm} - \omega)$ and the shift vector $R_{mn}^{a,b} = \partial_a \phi_{mn}^b - A_{mn}^a + A_{nn}^a$, where m and n are band indices. The sign of the absorption rate is always positive, while under band inversion, the shift vector $R_{mn}^{a,b}$ changes to $R_{nm}^{a,b}$ with a sign change. Hence, one expects that TPT prefers to flip the shift-current direction. This simple assumption is consistent with calculations in the second TPT in our system [Fig. 3(b)]. However, it is oversimplified for the first TPT, where the shift-current direction is not changed [Fig. 3(a)].

The phenomenon that the distinct shift-current direction behavior across two TPTs is witnessed, we further elaborate on the possible mechanism below. The k -resolved shift vector $R_{cv}(k)$ in the BZ, including the highest valence and the lowest conduction bands, are plotted for the $\varepsilon = 2.2$ and 2.3%, as shown in Figs. 4(a) and 4(b), respectively. The gap-closing k points are marked as 1, 2, and 3. For clarity reason, we plot shift-vector curves along k_y passing through these points in Figs. 4(c) and 4(d). It can be seen that the shift vector $R_{cv}(k)$ reverses its sign across the first TPT when the strain changes

from 2.2 to 2.3%. This indicates that the shift-vector $R_{cv}(k)$ sign is locked with band inversion during TPT. We compare the k -resolved shift current for strains of 0.9% ($Z_2 = 0$) and 4% ($Z_2 = 1$) with incident light at the corresponding band gap [$\hbar\omega = 0.053$ and 0.037 eV in Figs. 4(e) and 4(f)] and at the K point [$\hbar\omega = 0.090$ and 0.065 eV in Figs. 4(g) and 4(h)]. Figure 4(i) shows the enlarged shift-current distribution around K . After TPT, the shift vector $R_{cv}(k)$ indeed flips its sign around TPT points [Figs. 4(i-1) and 4(i-2)], but the absorption rate is negligibly small compared with that around K [Figs. 4(i-3) and 4(i-4)], where no band inversion occurs. It coincides with the fact that the peak keeps moving towards lower frequency after the band-gap reopening [Fig. 3(a)], different from the picture presented in Ref. [7]. This is due to the large shift-current contribution around K , at which the band gap continues to decrease towards the second TPT. However, one should note that k points in BZ contribute differently [41] to the shift current as the absorption rate $|r_{mn}^b|^2 \delta(\omega_{nm} - \omega)$ is k dependent. With an intensive band-structure study across the first TPT, we find that there is van Hove singularity near the valence- and conduction-band edge at K [Figs. 2(a)–2(f)], which leads to a much larger JDOS than the TPT points (Fig. S5 [35]). Thus, the main contribution to the shift current is from K , rather than the generic band-edge momenta for the first TPT.

In comparison, the shift-current behavior at the second TPT agrees well with previous conclusions [7]. The band inversion occurs at K , where the shift vector flips its sign [Figs. 4(j) and 4(k)]. The bands around K also contribute to the shift current [Figs. 4(l) and 4(m)]. The photon energy adopted in Figs. 4(j)–4(m) is the same as the band gap at the K point for $\varepsilon = 7$ and 10%.

Finally, we compare the value of the shift-current conductance of ReC_2H with previously proposed 2D systems: $\sim 150 \text{ \AA} \cdot \mu\text{A}/\text{V}^2$ for GeS (at a photon energy of ~ 2.500 eV) [41,42], $\sim 700 \text{ \AA} \cdot \mu\text{A}/\text{V}^2$ for WS_2 [41] (at an excitation energy of ~ 2.719 eV), $220 \mu\text{A}/\text{V}^2$ for Bi (110) monolayer (at a photon energy of 0.670 eV) [43], and $\sim 8 \mu\text{A}/\text{V}^2$ for 2H MoS_2 monolayer (with the photon energy of 2.800 eV) [44]. Thus, we note that the shift-current conductivity is quite large for the ReC_2H monolayer.

III. DISCUSSION

In conclusion, we investigate the interplay between TPT and NLO shift current generation in a 2D noncentrosymmetric ReC_2H monolayer. Under tensile biaxial strain, the band inversion emerges twice at generic momenta and K , respectively, which enables a topologically trivial-nontrivial-trivial phase transition with the critical strain of 2.3 and 7.8%. For its NLO response, the phenomenon of the enhanced shift-current conductivity at both TPTs is witnessed in line with other references. The shift current conductivity reaches $600 \text{ \AA} \cdot \mu\text{A}/\text{V}^2$ at an incident photon energy of 0.070 eV, comparable to previous proposed 2D materials. Remarkably, the shift current reverses direction at the second TPT but not at the first TPT. Our system with two TPTs offers a material realization, which evidences that TPT is accompanied by the shift-vector sign change but does not necessarily flip the direction of the shift current. Thus, a careful analysis is required in utilizing shift

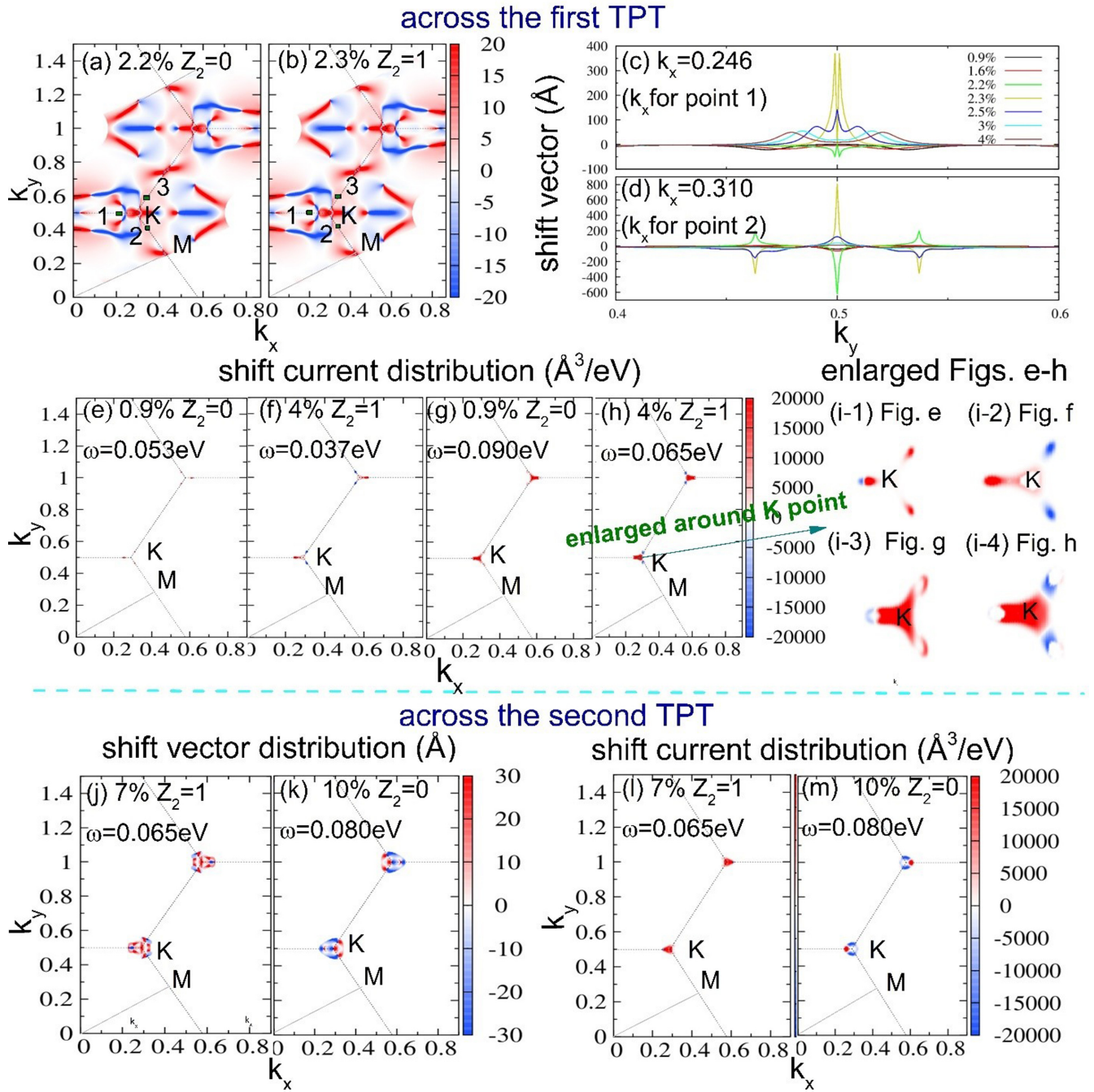


FIG. 4. (a), (b) The shift-vector distribution $R_{cv}(k)$ for ReC_2H monolayer with $\varepsilon = 2.2$ and 2.3% , which only includes the contribution from the highest valence- and the lowest conduction bands. The marked points 1, 2, and 3 are along K - M line, which are close to the first TPT point. (c), (d) The shift-vector distribution along k_y with specified k_x value the same as those of points 1 and 2. (e)–(h) Distribution of shift current in the whole BZ for $\varepsilon = 0.9$ and 4% . The incident light with excitation energy ($E_{nm} = \hbar\omega_{nm}$) of 0.053 and 0.037 eV (which is the band gap near TPT point), and 0.090 and 0.065 eV (band gap at K point) are used for $\varepsilon = 0.9$ and 4% , respectively. (i) The enlarged plots of shift-current distribution around K for $\varepsilon = 0.9$ and 4% . Distribution of (j), (k) shift vector and (i)–(m) shift current in the whole BZ for $\varepsilon = 7$ and 10% . The incident light with excitation energy of 0.065 and 0.080 eV are used, being the same as the band gap at K for $\varepsilon = 7$ and 10% .

current to detect TPT. On the other hand, if the k -resolved shift vector could be measured by some experimental technique, it would be a promising approach to characterizing TPT. Other optical rectification processes are not included in this study, and their effects will be discussed elsewhere. The combi-

nation of inversion-asymmetric polar TI, giant NLO effect, and the relationship between TPT and shift current could generate considerable impact in the fields of optical detector and sensor, energy harvesting and transfer, and terahertz wave generation.

IV. METHODS

The DFT calculations are performed with the QUANTUM ESPRESSO package [45], using the projector augmented-wave method [46] in PSLIBRARY [47], the Perdew-Burke-Ernzerhof exchange-correlation functional [48], and a plane-wave basis set with an energy cutoff of 60 Ry for valence electrons. A vacuum space of about 15 Å along the z direction is adopted to eliminate the artificial layer interactions. The BZ integration is sampled by using Γ -centered Monkhorst-Pack k -point sampling with a grid of $11 \times 11 \times 1$. The van der Waals interaction is described by the DFT-D3 method [49]. The WANNIER90 code package [50,51] is adopted to construct the tight-binding model based on the maximally localized Wannier functions. The edge states are calculated using the WANNIERTOOLS software package based on the semi-infinite Green function method [52]. The Wannier interpolation method [53] is adopted to calculate shift-current conductance using a refined k grid of $2000 \times 2000 \times 1$. The broadening factor of the delta function is adopted to be 0.02 eV. The k -point interpolation meshes are tested to obtain the well-converged shift-current results. The SOC is included self-consistently throughout the calculations. The IRs of electronic bands are calculated in the *irvsp* code [54]. In order to explore the dynamic stability, phonon dispersion is obtained by the finite-displacement method [55] as implemented in the PHONOPY code [56]. The AIMD simulations are carried out with a canonical ensemble at temperature of 300 and 500K for 10 ps with a time step of 1 fs [57]. Geometry relaxation and electronic structure calculations are also performed using the

Vienna *Ab initio* Simulation Package (VASP), and consistent results are obtained [46,58,59].

In time-reversal symmetry systems, under linearly polarized light with alternating electric field E at frequency ω , the shift-current conductivity is evaluated via [12,53] $\sigma_{bb}^a(\omega) = \frac{\pi e^3}{\hbar^2} \int \frac{d^3k}{8\pi^3} \sum_{m,n} f_{m,n} R_{mn}^{a;b} |r_{mn}^b|^2 \delta(\omega_{nm} - \omega)$, where light is polarized along the b direction. $f_{m,n} = f(E_n) - f(E_m)$ is the difference of Fermi-Dirac occupation, r_{mn}^b is interband Berry connections defined as $r_{mn}^b = i\langle m | \partial_{k_a} n \rangle$, $R_{mn}^{a;b} = \partial_a \phi_{mn}^b - A_{mn}^a + A_{mn}^a$ is the shift vector, and ϕ_{mn}^b is the phase of $r_{mn}^b = |r_{mn}^b| e^{i\phi_{mn}^b}$. $R_{mn}^{a;b}$ has the unit of length and can be physically interpreted as position change of a wave packet during its transition from band m to band n . The $|r_{mn}^b|^2 \delta(\omega_{nm} - \omega)$ evaluates absorption rate from band m to band n according to Fermi's golden rule.

ACKNOWLEDGMENTS

We acknowledge the financial support from the National Natural Science Foundation of China (NSFC) under Grants No. 12004306, No. 11974270, No. 11925408, and No. 12188101, the Ministry of Science and Technology of China (Grant No. 2018YFA0305700), the Chinese Academy of Sciences (Grant No. XDB33000000), the K. C. Wong Education Foundation (Grant No. GJTD-2018-01), the Beijing Natural Science Foundation (Grant No. Z180008), and the Beijing Municipal Science and Technology Commission (Grant No. Z191100007219013).

The authors declare no competing financial interest.

-
- [1] S. Murakami, S. Iso, Y. Avishai, M. Onoda, and N. Nagaosa, Tuning phase transition between quantum spin Hall and ordinary insulating phases, *Phys. Rev. B* **76**, 205304 (2007).
- [2] J. L. Collins *et al.*, Electric-field-tuned topological phase transition in ultrathin Na₃Bi, *Nature (London)* **564**, 390 (2018).
- [3] Y. Xu, Z. Song, Z. Wang, H. Weng, and X. Dai, Higher-Order Topology of the Axion Insulator EuIn₂As₂, *Phys. Rev. Lett.* **122**, 256402 (2019).
- [4] H. Huang and F. Liu, A unified view of topological phase transition in band theory, *Research* **2020**, 7832610 (2020).
- [5] J. Zhao, R. Yu, H. Weng, and Z. Fang, Topological node-line semimetal in compressed black phosphorus, *Phys. Rev. B* **94**, 195104 (2016).
- [6] H. Weng, X. Dai, and Z. Fang, Transition-metal Pentatelluride ZrTe₅ and HfTe₅: A Paradigm for Large-Gap Quantum Spin Hall Insulators, *Phys. Rev. X* **4**, 011002 (2014).
- [7] L. Z. Tan and A. M. Rappe, Enhancement of the Bulk Photovoltaic Effect in Topological Insulators, *Phys. Rev. Lett.* **116**, 237402 (2016).
- [8] C. Qian, C. Yu, S. Jiang, T. Zhang, J. Gao, S. Shi, H. Pi, H. Weng, and R. Lu, Role of Shift Vector in High Harmonic Generation from Noncentrosymmetric Topological Insulators under Strong Laser Fields, *Phys. Rev. X* **12**, 021030 (2022).
- [9] H. Xu, H. Wang, J. Zhou, Y. Guo, J. Kong, and J. Li, Colossal switchable photocurrents in topological Janus transition metal dichalcogenides, *NPJ Comput. Mater.* **7**, 31 (2021).
- [10] V. Belinicher, E. Ivchenko, and B. Sturman, Kinetic theory of the displacement photovoltaic effect in piezoelectrics, *Zh. Eksp. Teor. Fiz.* **83**, 649 (1982).
- [11] N. Kristoffel, R. Von Baltz, and D. Hornung, On the intrinsic bulk photovoltaic effect: Performing the sum over intermediate states, *Z. Phys. B: Condens. Matter* **47**, 293 (1982).
- [12] J. E. Sipe and A. I. Shkrebtii, Second-order optical response in semiconductors, *Phys. Rev. B* **61**, 5337 (2000).
- [13] R. von Baltz and W. Kraut, Theory of the bulk photovoltaic effect in pure crystals, *Phys. Rev. B* **23**, 5590 (1981).
- [14] L. Z. Tan, F. Zheng, S. M. Young, F. Wang, S. Liu, and A. M. Rappe, Shift current bulk photovoltaic effect in polar materials—hybrid and oxide perovskites and beyond, *NPJ Comput. Mater.* **2**, 16026 (2016).
- [15] I. Sodemann and L. Fu, Quantum Nonlinear Hall Effect Induced by Berry Curvature Dipole in Time-Reversal Invariant Materials, *Phys. Rev. Lett.* **115**, 216806 (2015).
- [16] J. E. Moore and J. Orenstein, Confinement-induced Berry Phase and Helicity-Dependent Photocurrents, *Phys. Rev. Lett.* **105**, 026805 (2010).
- [17] T. Morimoto and N. Nagaosa, Topological nature of nonlinear optical effects in solids, *Sci. Adv.* **2**, e1501524 (2016).
- [18] J. Ahn, G.-Y. Guo, and N. Nagaosa, Low-frequency Divergence and Quantum Geometry of the Bulk Photovoltaic Effect in Topological Semimetals, *Phys. Rev. X* **10**, 041041 (2020).

- [19] S. M. Young and A. M. Rappe, First Principles Calculation of the Shift Current Photovoltaic Effect in Ferroelectrics, *Phys. Rev. Lett.* **109**, 116601 (2012).
- [20] K. N. Okada, N. Ogawa, R. Yoshimi, A. Tsukazaki, K. S. Takahashi, M. Kawasaki, and Y. Tokura, Enhanced photogalvanic current in topological insulators via Fermi energy tuning, *Phys. Rev. B* **93**, 081403(R) (2016).
- [21] G. B. Osterhoudt *et al.*, Colossal mid-infrared bulk photovoltaic effect in a type-I Weyl semimetal, *Nat. Mater.* **18**, 471 (2019).
- [22] J. Ma *et al.*, Nonlinear photoresponse of type-II Weyl semimetals, *Nat. Mater.* **18**, 476 (2019).
- [23] Q. Xu, Y. Zhang, K. Koepf, W. Shi, J. van den Brink, C. Felser, and Y. Sun, Comprehensive scan for nonmagnetic Weyl semimetals with nonlinear optical response, *NPJ Comput. Mater.* **6**, 32 (2020).
- [24] H. Xu, J. Zhou, H. Wang, and J. Li, Giant photonic response of Mexican-hat topological semiconductors for mid-infrared to terahertz applications, *J. Phys. Chem. Lett.* **11**, 6119 (2020).
- [25] A. M. Cook, B. M. Fregoso, F. D. Juan, S. Coh, and J. E. Moore, Design principles for shift current photovoltaics, *Nat. Commun.* **8**, 14176 (2017).
- [26] L. V. Hove, The occurrence of singularities in the elastic frequency distribution of a crystal, *Phys. Rev.* **89**, 1189 (1953).
- [27] T. Zhang, Y. Jiang, Z. Song, H. Huang, Y. He, Z. Fang, H. Weng, and C. Fang, Catalogue of topological electronic materials, *Nature (London)* **566**, 475 (2019).
- [28] J. Zhou, Q. Wang, Q. Sun, X. Chen, Y. Kawazoe, and P. Jena, Ferromagnetism in semihydrogenated graphene sheet, *Nano Lett.* **9**, 3867 (2009).
- [29] M. Yang, D. Wouters, M. Giesbers, U. S. Schubert, and H. Zuilhof, Local probe oxidation of self-assembled monolayers on hydrogen-terminated silicon, *ACS Nano* **3**, 2887 (2009).
- [30] B. Fabre, Ferrocene-terminated monolayers covalently bound to hydrogen-terminated silicon surfaces. Toward the development of charge storage and communication devices, *Acc. Chem. Res.* **43**, 1509 (2010).
- [31] G. Scappucci, G. Capellini, W. Lee, and M. Simmons, Atomic-scale patterning of hydrogen terminated Ge (001) by scanning tunneling microscopy, *Nanotechnology* **20**, 495302 (2009).
- [32] E. Bianco, S. Butler, S. Jiang, O. D. Restrepo, W. Windl, and J. E. Goldberger, Stability and exfoliation of germanane: A germanium graphane analogue, *ACS Nano* **7**, 4414 (2013).
- [33] Y. Li, K. Chang, Z. Sun, E. Shangguan, H. Tang, B. Li, J. Sun, and Z. Chang, Selective preparation of 1T-and 2H-phase MoS₂ nanosheets with abundant monolayer structure and their applications in energy storage devices, *ACS Appl. Energy Mater.* **3**, 998 (2019).
- [34] Y. Hwang and N. Shin, Hydrogen-assisted step-edge nucleation of MoSe₂ monolayers on sapphire substrates, *Nanoscale* **11**, 7701 (2019).
- [35] See Supplemental Material at <http://link.aps.org/supplemental/10.1103/PhysRevB.105.245108> for phonon spectra, AIMD, band structure without SOC, whole band structure and Z2 changes of strained ReC₂H monolayer, the evolution lines of Wannier charge centers along KZ = 0 plane, matrices of the representations of the little group at the K point, zigzag edge state of one-dimensional projection for the two-dimensional BZ for strained ReC₂H monolayer, The shift-current peak position corresponding to the bands transition, joint density of states of ReC₂H monolayer, and the orbital component weight analyses around topological phase transition point.
- [36] Z. Y. Zhu, Y. C. Cheng, and U. Schwingenschlöggl, Giant spin-orbit-induced spin splitting in two-dimensional transition-metal dichalcogenide semiconductors, *Phys. Rev. B* **84**, 153402 (2011).
- [37] L. Fu and C. L. Kane, Topological insulators with inversion symmetry, *Phys. Rev. B* **76**, 045302 (2007).
- [38] R. Yu, X. L. Qi, A. Bernevig, Z. Fang, and X. Dai, Equivalent expression of Z₂ topological invariant for band insulators using the non-Abelian Berry connection, *Phys. Rev. B* **84**, 075119 (2011).
- [39] Y. Qian, Z. Tan, T. Zhang, J. Gao, Z. Wang, Z. Fang, C. Fang, and H. Weng, Layer construction of topological crystalline insulator LaSbTe, *Science China Phys., Mech.* **63**, 107011 (2020).
- [40] L. Wu, S. Patankar, T. Morimoto, N. L. Nair, E. Thewalt, A. Little, J. G. Analytis, J. E. Moore, and J. Orenstein, Giant anisotropic nonlinear optical response in transition metal monopycnitide Weyl semimetals, *Nat. Phys.* **13**, 350 (2017).
- [41] C. Wang, X. Liu, L. Kang, B.-L. Gu, Y. Xu, and W. Duan, First-principles calculation of nonlinear optical responses by Wannier interpolation, *Phys. Rev. B* **96**, 115147 (2017).
- [42] T. Rangel, B. M. Fregoso, B. S. Mendoza, T. Morimoto, J. E. Moore, and J. B. Neaton, Large Bulk Photovoltaic Effect and Spontaneous Polarization of Single-Layer Monochalcogenides, *Phys. Rev. Lett.* **119**, 067402 (2017).
- [43] Y. Pan and J. Zhou, Toggling Valley-Spin Locking and Nonlinear Optical Properties of Single-Element Multiferroic Monolayers via Light, *Phys. Rev. Applied* **14**, 014024 (2020).
- [44] A. M. Schankler, L. Gao, and A. M. Rappe, Large bulk piezophotovoltaic effect of monolayer 2H-MoS₂, *J. Phys. Chem. Lett.* **12**, 1244 (2021).
- [45] P. Giannozzi *et al.*, QUANTUM ESPRESSO: A modular and open-source software project for quantum simulations of materials, *J. Phys.: Condens. Matter* **21**, 395502 (2009).
- [46] P. Blöchl, Generalized gradient approximation made simple, *Phys. Rev. B: Condens. Matter Mater. Phys.* **50**, 17953 (1994).
- [47] A. Dal Corso, Pseudopotentials periodic table: From H to Pu, *Comput. Mater. Sci.* **95**, 337 (2014).
- [48] J. P. Perdew, K. Burke, and M. Ernzerhof, Generalized Gradient Approximation Made Simple, *Phys. Rev. Lett.* **77**, 3865 (1996).
- [49] S. Grimme, Semiempirical GGA-type density functional constructed with a long-range dispersion correction, *J. Comput. Chem.* **27**, 1787 (2006).
- [50] A. A. Mostofi, J. R. Yates, G. Pizzi, Y.-S. Lee, I. Souza, D. Vanderbilt, and N. Marzari, An updated version of wannier90: A tool for obtaining maximally-localised Wannier functions, *Comput. Phys. Commun.* **185**, 2309 (2014).
- [51] A. A. Mostofi, J. R. Yates, Y.-S. Lee, I. Souza, D. Vanderbilt, and N. Marzari, wannier90: A tool for obtaining maximally-localised Wannier functions, *Comput. Phys. Commun.* **178**, 685 (2008).
- [52] Q. Wu, S. Zhang, H.-F. Song, M. Troyer, and A. A. Soluyanov, WannierTools: An open-source software package for novel topological materials, *Comput. Phys. Commun.* **224**, 405 (2018).
- [53] J. Ibanez-Azpiroz, S. S. Tsirkin, and I. Souza, Ab initio calculation of the shift photocurrent by Wannier interpolation, *Phys. Rev. B* **97**, 245143 (2018).

- [54] J. Gao, Q. Wu, C. Persson, and Z. Wang, Irvsp: To obtain irreducible representations of electronic states in the VASP, *Comput. Phys. Commun.* **261**, 107760 (2021).
- [55] K. Parlinski, Z. Q. Li, and Y. Kawazoe, First-Principles Determination of the Soft Mode in Cubic ZrO₂, *Phys. Rev. Lett.* **78**, 4063 (1997).
- [56] A. Togo, F. Oba, and I. Tanaka, First-principles calculations of the ferroelastic transition between rutile-type and CaCl₂-type SiO₂ at high pressures, *Phys. Rev. B* **78**, 134106 (2008).
- [57] C. Zhang, L. Zhang, C. Tang, S. Sanvito, B. Zhou, Z. Jiang, and A. Du, First-principles study of a Mn-doped in 2Se₃ monolayer: coexistence of ferromagnetism and ferroelectricity with robust half-metallicity and enhanced polarization, *Phys. Rev. B* **102**, 134416 (2020).
- [58] G. Kresse and J. Hafner, Ab initio molecular dynamics for liquid metals, *Phys. Rev. B* **47**, 558 (1993).
- [59] G. Kresse and J. Furthmüller, Efficient iterative schemes for ab initio total-energy calculations using a plane-wave basis set, *Phys. Rev. B* **54**, 11169 (1996).